An Electric Induction Micromotor

Steven F. Nagle, *Member, IEEE*, Carol Livermore, *Member, IEEE*, Luc G. Frechette, Reza Ghodssi, *Member, IEEE*, and Jeffrey H. Lang, *Fellow, IEEE*

Abstract—This paper presents the analysis, design, fabrication, and testing of a planar electric induction micromotor. The micromotor is a 6-phase motor with 131 pole pairs distributed on a stator having a 4 mm outer diameter. The axial air gap is 3 μm. With a 90 V stator excitation, applied at a 300-kHz slip frequency, the motor produces a torque of 2 μN $\cdot$ m. Special attention is paid to the limitations that microfabrication places on the design of the motor. **[1086]**

Index Terms—Deep reactive ion etching (DRIE), duffing oscillator, electrostatic actuator modeling design analysis, micromotor, power microelectromechanical systems (Power MEMS) fabrication, quasi-static electric induction machine motor generator, torque measurement.

I. INTRODUCTION

PORTABLE electronics will continue to shrink. Small, lightweight electronic systems have been the goal of many leading-edge high-technology efforts for certain industries, including aerospace, telecommunications, and biotechnology, over the past 30 years. When current battery technology shrinks, it's power output can become unacceptable. An obvious approach to this problem is power conservation, but it is fair to say that all portable electronics strive to minimize their power budget. This approach also generally limits the functionality of the system. Approaching the problem from a different angle, several research programs are developing radical changes in the core technology: these include microscale fuel cells, microscale nuclear batteries, and microscale generators driven by internal combustion. One such program seeks to produce a microscale gas-turbine generator capable of producing tens of watts of electrical power [1], [2]. The generator provides the motivation for this paper. While a variety of microscale electric and magnetic machines could be developed for the generator, we believe that an electric induction machine[1] is the best choice. This paper details the development of a microscale electric induction machine, and focuses on measurements of its performance as a motor, rather than a generator, for reasons described below.

Many publications can be found on the theory and fabrication of electric and magnetic machines, but very few microscale versions of these machines have been successfully applied to practical problems. We have decided to pursue only one of these machines in the context of the gas turbine generator for a variety of reasons. First, we eliminate magnetic machines because their processing is not generally compatible with the standard CMOS processing tool set used for the rest of the microscale gas turbine, and because magnetic materials may not withstand the high temperatures expected during engine operation.[2] Further, their rotors are fundamentally heavy and make the design of successful high-speed air bearings very challenging. Second, we eliminate machines that require rotor contact, such as elastodynamic machines and brushed machines. These include, but are not limited to, ultrasonic motors, vibromotors, and scratch-drive motors. Excessive friction reduces their torque, and wear limits their life, in the high speed environment of the microgenerator [3]. This is unfortunate since these machines generally produce the most torque. Third, we eliminate corona machines because corona discharge would be unwise in the presence of the fuel vapors in the environment of the microgenerator. Fourth, we eliminate permanent machines because they are synchronous, because permanent magnet machines have issues described above, and because permanent electrets are not particularly stable at elevated temperatures and do not appear to be capable of high performance in practice [4]. Finally, we eliminate variable-capacitance machines because they are synchronous machines and as such would require position information for high-performance operation. Position information is difficult to obtain from within the microgenerator, and torque decreases rapidly with less than perfect synchronization. Thus, we believe that the asynchronous electric induction machine is the best choice for the microgenerator.

As a precursor to generator development, this paper describes the design, fabrication, and testing of a microscale electric induction motor. It does so for three reasons. First, the models developed here are equally applicable to generator and motor

[1]Note that in most electric machine literature, what is referred to as an electric induction machine is in fact a magnetic induction machine. The term electric induction machine is used here to refer to the electric dual of the magnetic induction machine, also referred to as a quasi-static electric induction machine, or an electrostatic induction machine.

[2]This option has recently been explored with encouraging results [25], [26], but the fundamental incompatibilities remain.
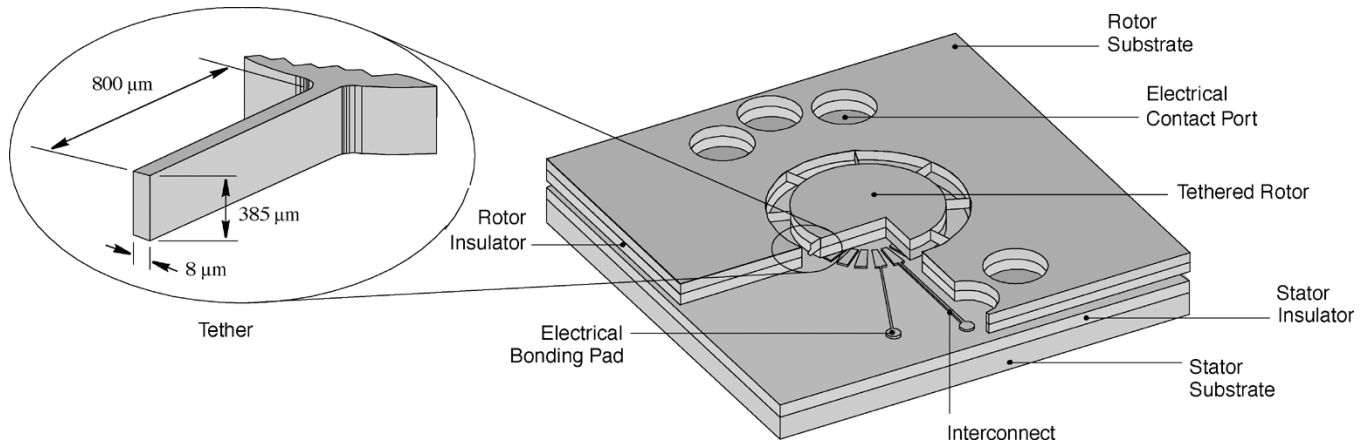
Fig. 1. Illustration of the tethered motor. The size of the electrodes is greatly exaggerated, their number is greatly reduced, and the phase buses are not shown. The buses and other features can be seen in two fabricated devices shown in Figs. 11, 12, and 13.

operation; validating one use validates the other. Second, motoring behavior is much easier to measure because the rotor need not spin, and therefore need not be supported by bearings that introduce fabrication complexity and operating losses. Instead, the rotor fabricated here is suspended over the stator on spring tethers. In this way, rotor torque can be accurately measured through tether bending. Finally, the micromotor described here provides a means to power a microcompressor and therefore test the design of the microcompressor. Such a microcompressor could have a variety of applications, including the compressor at the inlet of fuel cells or the compressor for the gas-turbine in a microgenerator [18].

This paper offers at least three contributions to the literature. First, this paper describes the first fabrication and testing of a microscale electric induction motor. Earlier papers have described their operation [12], and larger electric induction motors have been analyzed, fabricated, and tested by several authors [6]–[9]. Second, this paper focuses on the design and optimization of the electric induction machine as restricted by microfabrication. While the electric induction machine has been studied in [10] and [11], and more recently in [9], [12], and [13], the prior literature does not focus on the design and optimization of microfabricated machines. Finally, a metrology technique to directly measure micromotor torque is presented. The rotor is suspended over the stator using integrated spring tethers, and so the motor is referred to as a tethered motor. Although spring loads have been used to test the performance of macroscale motors, the technique has not yet been used for microscale motors.

The paper begins with a description of electric induction machines and their operating principles. Then, Section III develops models for planar rotary machines. Section IV focuses on design optimization in the context of motoring operation, with particular attention paid to three parameters that strongly affect performance and are in turn limited by microfabrication constraints. Section V briefly outlines tethered motor fabrication. Section VI describes torque measurements, and compares these measurements to values predicted by the models of Section III. Finally, the last section provides a summary and conclusions.

II. ELECTRIC INDUCTION MACHINES

The tethered electric induction motor studied here is a planar 6-phase motor constructed as shown in Fig. 1. The planar geometry is chosen to be compatible with microfabrication. The rotor and stator are 4 mm in diameter and separated by a gap of 3 μm. The stator contains 768 radial electrodes, separated by a 4-μm space along their radial length. Each is in contact with one of six separate phase buses, connected by a via of 2-μm diameter passing through a 1-μm-thick interlevel oxide. The electrodes are supported by an insulation layer that is as thick as can be reliably fabricated. The rotor comprises a 0.5-μm sheet of moderately doped polysilicon deposited on a 10-μm-thick oxide insulation layer that is deposited on a 400-μm-thick silicon wafer. The rotor is tethered above the stator by eight silicon springs etched from the silicon wafer. A more complete listing of design parameters for this tethered motor is given in Table I; many of the parameters are defined in Section III.

During motoring operation, external electronics excite the stator electrodes to produce a potential wave which travels around the stator with a speed exceeding that of the rotor. The corresponding distribution of charges on the stator electrodes induces image charges on the rotor surface across the air gap. The speed of the traveling stator potential and charge waves exceeds the mechanical speed of the rotor, so convection alone cannot synchronize the rotor charges with the stator charges. Since the charge and potential waves must be synchronized in steady state the rotor charges must conduct through the stationary tethered rotor. In our motor the charges conduct through a thin film on an otherwise insulating rotor; the 0.5-μm polysilicon film is referred to here as the rotor conductor. The conduction process must in turn be driven by a tangential electric field, and so the rotor charges lag behind the stator waves to produce that field, as shown in Fig. 2. Finally, the tangential electric field acts on the rotor charges to impart a tangential surface stress on the rotor, which in turn results in a motoring torque. Conversely, during generating operation, the rotor speed exceeds that of the traveling stator waves, and the process is reversed.

TABLE I
MODELED MOTOR PARAMETERS FOR THE BASELINE DESIGN AS WELL AS MEASURED PARAMETERS FOR THE TWO TESTED MOTORS.
IF THERE IS A '—' INSTEAD OF AN ENTRY, THEN THE VALUE IS INDIRECTLY DETERMINED IN SECTION VI

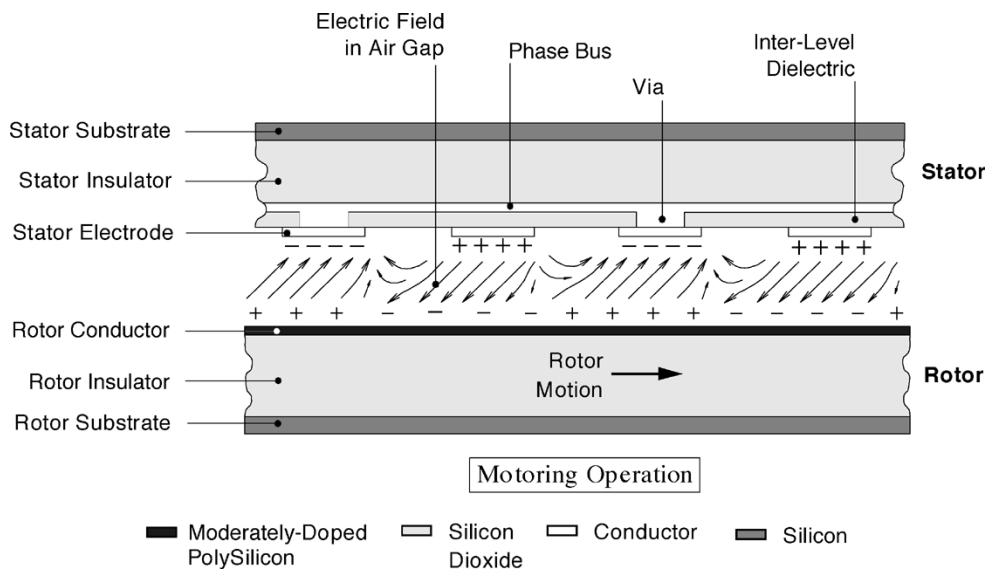| Parameter	Symbol	Baseline Design	Value in Device-1	Value in Device-2
Stator rated voltage amplitude	V_s	300 V	—	—
Stator applied voltage fundamental magnitude	$V = V_{11}$	285 V	77 V or 80 V	90 V
Stator excitation frequency	f_e	2.6 MHz	100 - 800 kHz	300 kHz
Stator insulator thickness	Δ_{si}	10 μm	5 μm	500 μm
Stator insulator (SiO$_2$) permittivity	ε_{si}	$3.9\varepsilon_o$	$3.9\varepsilon_o$	$3.9\varepsilon_o$
Stator periodicity	m	131	131	131
Number of phases		6	6	6
Number of electrodes		786	786	786
Electrode inner radius		1 mm	1 mm	1 mm
Electrode outer radius		2 mm	2 mm	2 mm
Electrode inner width		4 μm	4 μm	4 μm
Electrode outer width		11 μm	11 μm	11 μm
Stator electrode thickness		1 μm	1 μm	0.3 μm
Inter-electrode gap		4 μm	4 μm	4 μm
Stator-rotor air gap length	G	3 μm	—	—
Air gap permittivity	ε_g	ε_o	ε_o	ε_o
Slip	s	—	—	—
Rotor conductor sheet resistance	ρ_{rcs}	200 MΩ	—	—
Rotor synchronous speed	Ω_{sync}	1.2×10^6 rpm	0	0
Rotor insulator thickness	Δ_{ri}	10 μm	10 μm	10 μm
Rotor mass	M_r	NA	13 mg	13 mg
Rotor disk radius	R_r	NA	2.1 mm	2.1 mm
Rotor conductor inner radius	R_i	1 mm	1 mm	1 mm
Rotor conductor outer radius	R_o	2 mm	2 mm	2 mm
Rotor insulator (SiO$_2$) permittivity	ε_{ri}	$3.9\varepsilon_o$	$3.9\varepsilon_o$	$3.9\varepsilon_o$
Rotor insulator (SiO$_2$) resistivity	ρ_{ri}	1.0×10^{14} Ω-cm	1.0×10^{14} Ω-cm	1.0×10^{14} Ω-cm
Rotor conductor thickness	δ_{rc}	0.5 μm	0.5 μm	0.5 μm
Tether length		850 μm	—	—
Tether height		386.5 μm	—	—
Tether width		8.0 μm	—	—
Number of tethers		8	3	3

Fig. 2. Side-view illustration looking radially outward that shows a greatly simplified representation of the electric field in the air gap during motoring operation.
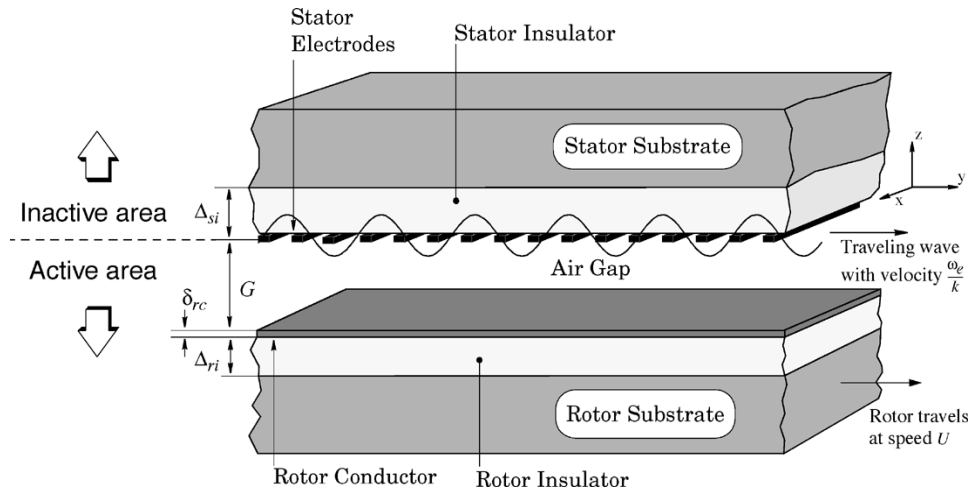
Fig. 3.   A perspective view of a 2-D representation of the interior of the electric induction motor. Only the active area affects torque production because the electrode potential is enforced on the dividing plane. This paper does not consider the inactive area.

The stator and rotor charge waves travel at the same speed, but as alluded to above, in order to develop torque the rotor surface must travel at a different speed. The difference between these two speeds is the slip speed. The time over which the rotor waves travel one charge distribution wavelength through the rotor is the reciprocal of the slip frequency. In the case of the tethered motor studied here, the electrical frequency of the stator and the slip frequency are the same because the rotor is stationary. The electric induction machine performs best when the product of its rotor charge relaxation time constant and the slip frequency is unity. This is demonstrated below in Section III via (10), (12), (13), and (16). If the charge relaxation time is too long, or the slip frequency is too high, then little rotor charge develops and torque is reduced. If the charge relaxation time is too short, or the slip frequency is too low, then the rotor charges align beneath the stator charges and the electric field between them is nearly axial. The tangential component of the electric field, and hence the rotor torque, is again reduced [5], [20]. Nevertheless, a substantial tangential component exists over a broad range of rotor speeds, resulting in good torque over the same range. Since the electric induction machine is an asynchronous machine, neither rotor speed nor rotor position information is required for good performance, as shown ahead in Fig. 7 and in Fig. 16.

The first electric induction motor, a macroscale machine, may have been fabricated over 100 years ago by Arno [22]. Bollee [6] believed that Arno's motor exploited dielectric hysteresis in the glass and ebony rotors that he used, so in current usage of the term this would not be an induction machine. However it is likely that Arno's rotor surface was not perfectly clean; it is commonly accepted that simply touching a perfect insulator with bare hands will impart it with at most a 1-GΩ sheet resistance. Thus, it is possible that Arno's machine did employ free charge conduction, as exhibited in an electric induction machine. Since Arno's time research on electric induction machines has grown slowly, as Bollee and other authors have also noted [6], [8], [12]. Macroscale versions were fabricated 30 years ago, and measurements of the starting torque were made as a function of excitation frequency [6], [7]. Building upon these results, other researchers fabricated similar electric

induction motors more recently [8], [9]. Some also advanced the study of nonideal effects inherent to this machine type [8], [23]. Still, none of these efforts yielded practical motors which could be employed for the purposes of [1], [2]. This paper presents the development of microscale electric induction motors that could be employed for those purposes and are capable of rotor torque densities on the same order of magnitude as macroscale magnetic induction motors. This paper presents demonstration of rotor torque one order of magnitude less than that, limited by power electronics.

III. MODEL DEVELOPMENT

The electric induction machine studied here encompasses a wide range of length scales. In fact, machine proportions are well represented by two coins separated by an air gap no larger than a single grain of pollen. Though it makes fabrication more difficult, this difference in scale greatly simplifies the models. On the scale of the air gap, the machine can be modeled as two parallel planes moving past each other in the manner of Fig. 3.

This section derives the tangential and normal forces generated by a rectilinear electric induction machine. Since all fields are invariant with respect to the x-coordinate direction in Fig. 3, this model is referred to as a 2-D model, with tangential and normal force expressions derived in a rectilinear coordinate system. This section then concludes by describing the conditions under which the rectilinear expressions can be adapted to the inherently 3D shape of the tethered motor shown in Fig. 1, and provides a torque expression in cylindrical coordinates.

Each stator electrode is excited using a periodic signal of amplitude V_s and frequency ω_e. Phase lag from one electrode to the next is uniformly spaced to implement a potential wave travelling along in the y-coordinate direction. With a stator excitation that is both spatially and temporally periodic, as shown by the illustration of Fig. 4, the travelling wave of potential imposed by the stator electrodes can be expressed as a sum of complex Fourier components of the form

$$\hat{\Phi} = \sum_n \sum_p \hat{V}_{pn} e^{j(pky - n\omega_e t)} \qquad (1)$$
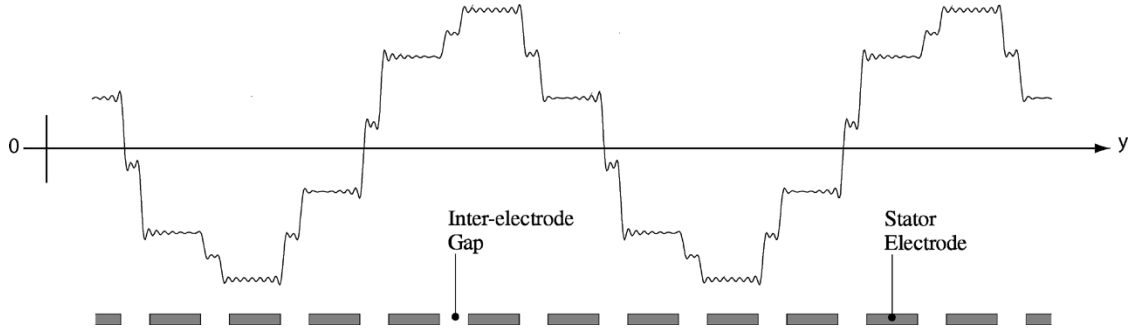
Fig. 4. Two spatial wavelengths of the stator potential at an instant in time. Here the potential across each inter-electrode gap is assumed to be the average of the electrode potentials on either side of the gap. Each stator electrode is excited using a pure sinusoidal signal of amplitude V_s.

where n and p are Fourier component indices, $\hat{V}_{pn}$ is the complex amplitude of the $[p, n]$ component, $k = 2\pi/\lambda$ is the fundamental spatial wavenumber, λ is the fundamental spatial wavelength, and $\omega_e = 2\pi f_e$ is the fundamental temporal stator excitation frequency. As a consequence, the electric potentials and fields within the electric induction machine will also take the form of a sum of Fourier components.

The Fourier sums can be truncated for ease of model development and description. In the present micromotors, each stator electrode excitation is reasonably sinusoidal in time. The regular spacing of six independent stator phases, sampling a sinusoidal function of potential around the stator at six points per wavelength, enforces a reasonably sinusoidal potential wave on the stator as shown by Fig. 4 and Fig. 5. Therefore, to simplify the explanation of the derivation in this section, (1) is truncated after only the fundamental component, $n = p = 1$, and the subscripts are dropped unless otherwise noted so that $\hat{V} = \hat{V}_{11}$. In addition, the magnitude of the fundamental component is defined as $V = |\hat{V}|$. The design analysis in Section IV is carried out using the fundamental temporal harmonic and all nonzero spatial harmonics whose magnitudes are plotted in Fig. 5, and the data analysis in Section VI is carried out using measured temporal harmonics and all spatial harmonics plotted in Fig. 5.

Since free volume charge is assumed to be nonexistent within the induction machine, Laplace's equation describes the complex electric potential $\hat{\phi}(x, y, z, t)$ within the rectilinear, 2-D electric induction machine shown in Fig. 3. Laplace's equations are solved using the standard solutions

$$\sinh(kz)e^{jky} \qquad (2)$$

obtained through variable separation. We choose two independent solutions, one to match each boundary in the induction machine. Thus the first solution $\hat{\phi}_g$ to Laplace's equation in the air gap, with $z = 0$ at the electrode surface and negative z pointing toward the rotor, is

$$\phi_g(x, y, z, t) = \frac{\hat{V} \sinh\left[k(z + G)\right] - \hat{\Phi}_{ri} \sinh(kz)}{\sinh(kG)} e^{j(ky - \omega_e t)} \qquad (3)$$

where $\hat{V}$ is the fundamental of the complex amplitude of the traveling potential wave on the stator, as described earlier, $\hat{\Phi}_{ri}$ is then the fundamental of the complex amplitude of the travelling potential wave at the rotor surface, ω_e is the stator temporal excitation frequency and k is the wavenumber, or spatial frequency, of the traveling wave. Additional details can be found
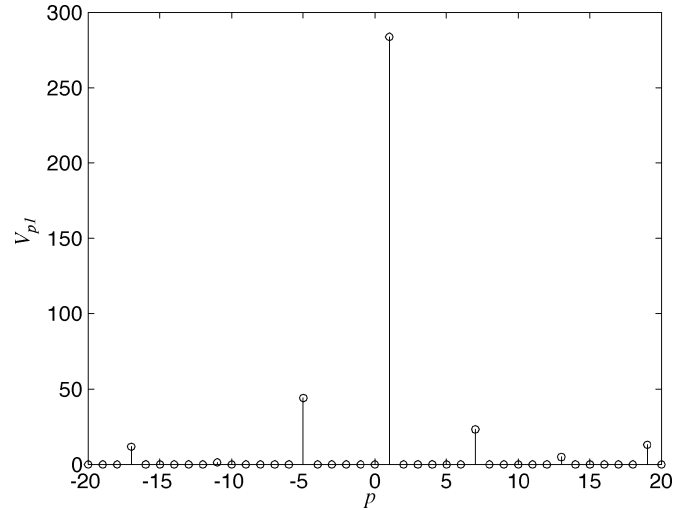

Fig. 5. The magnitude of the complex-valued potential spatial harmonics which correspond to a single applied temporal harmonic of stator potential, of amplitude $V_s = 300$ V. Note the size of the spatial fundamental of magnitude $V = V_{11} = 285$ V, in comparison to the first backward-traveling component and the first forward-traveling component.

in [5], [12], [19], [20]. A complete list of parameters is found in Table I.

The air gap potential $\hat{\phi}_g$ induces a potential in the rotor that is expressed with a second solution $\hat{\phi}_{ri}$ to Laplace's equation in the rotor insulator of the form

$$\phi_{ri}(x, y, z, t) = \frac{\hat{\Phi}_{ri} \sinh\left[k(z + G + \Delta_{ri})\right]}{\sinh(k\Delta_{ri})} e^{j(ky - \omega_e t)}. \qquad (4)$$

Note that this solution yields an induced potential at the rotor surface with a fundamental of $\hat{\Phi}_{ri}$. The potential is zero at the rotor substrate because the substrate is assumed to be perfectly conducting. The parameters G and Δ_{ri} refer to the air gap thickness and rotor insulator thickness, respectively, as shown in Fig. 3 and Table I. The rotor conductor thickness δ_{rc} is much less than λ.

Gauss' Law applied to the rotor surface can be used to determine $\hat{\rho}_{rc}$, the free surface charge on the rotor, according to

$$\hat{\rho}_{rc} = \left[\varepsilon_g \hat{E}_{g_z} - \varepsilon_{ri} \hat{E}_{ri_z}\right]\Big|_{z=-G} \qquad (5)$$

where $\hat{E}$ is the electric field obtained from

$$\hat{E} = -\nabla \hat{\phi} \qquad (6)$$

where ε_g is the permittivity of the air gap, and ε_{ri} is the permittivity of the rotor insulator. Next, charge conservation at the surface of the rotor may be expressed as

$$\left(\frac{\partial}{\partial t} + U\frac{\partial}{\partial y}\right)\hat{\rho}_{rc} + \sigma_{rcs}\frac{\partial \hat{E}_{ri_y}}{\partial y} + \sigma_{ri}\left.\frac{\partial \hat{\phi}_{ri}}{\partial z}\right|_{z=-G^-} = 0 \quad (7)$$

where $\sigma_{rcs} = \delta_{rc}\sigma_{rc}$ and σ_{ri} are the rotor conductor sheet conductivity and rotor insulator conductivity, respectively [5], [12], [19], [20]. The first term in (7) is simply the rate of change of charge in an infinitesimal volume collapsed around the rotor conductor surface, but fixed in space. The second term accounts for y-directed charge convection into or out of the volume, the third term accounts for y-directed conduction through the rotor conductor into or out of the volume, while the fourth term accounts for z-directed charge conduction through the rotor insulator into or out of the volume. The rotor insulator is not assumed to be a perfect insulator, the value used in the analysis below is listed in Table I.

Substitution of (3), (4), (5), and (6) into (7), with rearrangement of terms, leads to

$$\frac{1}{\omega_e}\left[k\sigma_{rcs} + \sigma_{ri}\coth(k\Delta_{ri})\right]\hat{\Phi}_{ri} = \frac{(\omega_e - kU)}{\omega_e}$$
$$\times\left[\frac{\varepsilon_g}{\sinh(kG)}\hat{V} - (\varepsilon_g\coth(kG) + \varepsilon_{ri}\coth(k\Delta_{ri}))\hat{\Phi}_{ri}\right]. \quad (8)$$

Equation (8) is solved for the rotor potential amplitude $\hat{\Phi}_{ri}$ to yield

$$\hat{\Phi}_{ri} = \beta \cdot \frac{j\tau_{R^s}\omega_e}{1 + j\tau_{R^s}\omega_e} \cdot \hat{V} = \beta[j - \Gamma]\cdot\frac{\Gamma}{1 + \Gamma^2}\cdot\hat{V} \quad (9)$$

where

$$s \equiv \frac{\omega_e - kU}{\omega_e} \quad (10)$$

is the slip, a normalized measure of the relative speed by which the electric field and potential waves "slip" through the rotor, parallel to its surface, in steady state. Several terms are grouped because of physical significance, these are

$$\beta(k) \equiv \frac{\varepsilon_g}{\varepsilon_{\text{eff}}(k)\sinh(kG)} \quad (11)$$
$$\Gamma \equiv \tau_{R^s}\omega_e \quad (12)$$

and

$$\tau_R \equiv \varepsilon_{\text{eff}}\rho_{\text{eff}} = \frac{\varepsilon_{eff}}{\sigma_{\text{eff}}}. \quad (13)$$

The last term is the rotor charge relaxation time constant expressed in terms of the effective permittivity of the rotor ε_{eff}, given by

$$\varepsilon_{\text{eff}}(k) = \varepsilon_g\coth(kG) + \varepsilon_{ri}\coth(k\Delta_{ri}) \quad (14)$$

the effective resistivity of the rotor ρ_{eff}, and the effective conductivity of the rotor σ_{eff}, both given in terms of the resistivities by

$$\sigma_{\text{eff}}(k) = \frac{1}{\rho_{\text{eff}}(k)} = \frac{k}{\rho_{rcs}} + \frac{\coth(k\Delta_{ri})}{\rho_{ri}}. \quad (15)$$

The term β is a measure of capacitive shunting of the electric field through the rotor substrate instead of through the rotor conductor. Capacitive shunting reduces performance and is described in more detail in Section IV. The term Γ is the ratio of the rotor charge relaxation time τ_R and what can be called the "slip period" $1/s\omega_e$. The slip period is the time required for the induced rotor charge distribution to travel one wavelength λ through the rotor conductor, parallel to the rotor surface velocity. The charge relaxation time is a typical RC time constant, i.e., an exponential decay time constant describing a transient relaxation of the charge distribution within the induction machine rotor. When these two times are equal, $\Gamma = 1$ and motive force is maximized, as seen in (16).

The results of the electric field analysis are next used in the Maxwell stress tensor [5], [20] to find the time- and space-average tangential force f_y on the rotor, per unit area. This force is given by

$$f_y = \frac{\varepsilon_g}{\lambda}\int_0^\lambda [E_yE_z]|_{z=-G}\,dy = \frac{\varepsilon_gV^2}{2}\cdot\frac{\Gamma}{1+\Gamma^2}\cdot\beta\cdot\frac{k^2}{\sinh(kG)}. \quad (16)$$

Similarly, the time- and space-average normal force f_z on the rotor, per unit area, is given by

$$f_z = \frac{\varepsilon_g}{2\lambda}\int_0^\lambda [E_zE_z - E_yE_y]|_{z=-G}\,dy$$
$$= \varepsilon_g\left[\frac{kV}{2\sinh(kG)}\right]^2$$
$$\cdot\frac{1 + \Gamma^2\left[\beta^2 - 2\beta\cos(kG) + 1\right]}{1 + \Gamma^2}. \quad (17)$$

The 2-D rectilinear single-harmonic solution is now converted to a 3-D annular single-harmonic solution using the coordinate transformation $x \to r$, $y \to r\theta$, $z \to z$. In effect, this coordinate transformation wraps a rectangular strip of the rectilinear electric induction machine, shown in Fig. 2 and Fig. 3, into an annular strip within a rotary machine, shown in Fig. 1 and Fig. 6(c). The cartesian coordinate system is thus mapped onto a cylindrical coordinate system. In doing so, it is assumed that an integral number of rectilinear wavelengths fit onto the annulus. That number is m and is hereafter called the periodicity. The accuracy of the mapping process depends on the degree of curvature encountered in the wrapping.

Quantitative bounds on the accuracy of the mapping follow from a mathematical treatment of the process. To begin, recall that a 2-D cartesian solution to Laplace's equation takes the form

$$\hat{\phi} \propto e^{\pm jky}e^{\pm kz} \quad (18)$$

since there is no dependence on x. To apply a solution of this form to a cylindrical geometry, it is necessary only to take advantage of the coordinate map shown in the left column of Fig. 6(d). The electric potential, for example, in cylindrical coordinates is then approximated by

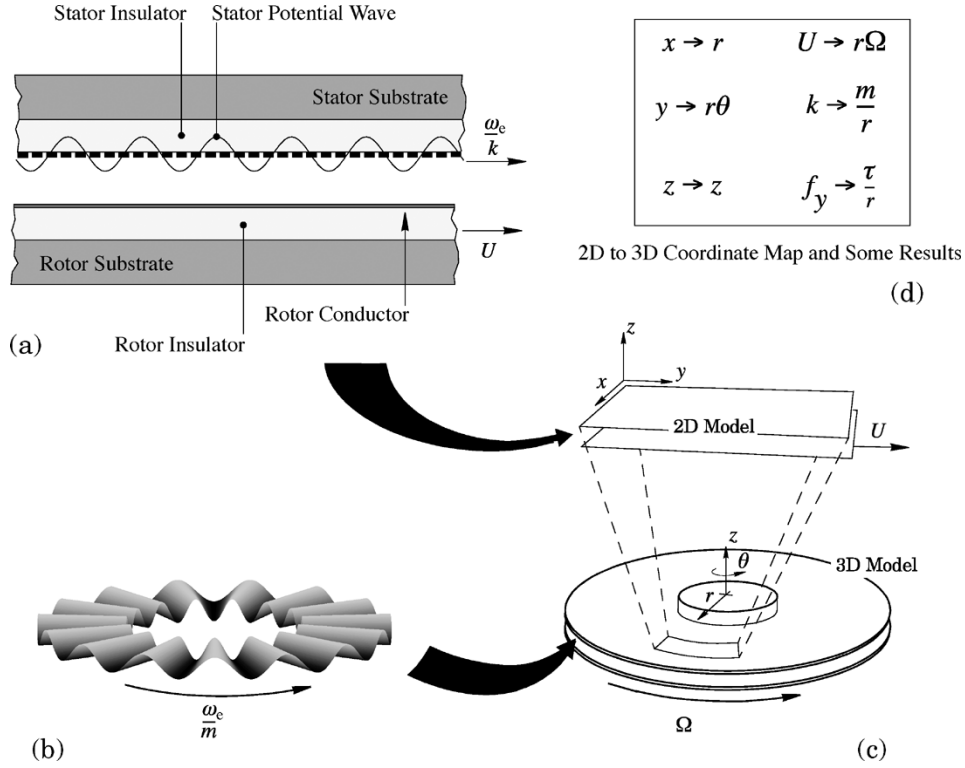$$\hat{\phi}^* \propto e^{\pm jm\theta}e^{\pm\frac{m}{r}z}. \quad (19)$$

Fig. 6. The process of mapping a 2-D single-harmonic model to a 3-D single-harmonic model. (a) A summary of the 2-D model. (b) The 3-D single-harmonic stator potential wave. (c) Depiction of the mapping process. (d) The coordinate map.

Here the superscript * denotes the approximation resulting from the mapping.

Equation (19) will be an appropriate approximation only within a certain range of the cylindrical coordinates r, θ, and z. To define this range, $\hat{\phi}^*$ is inserted into the cylindrical-coordinate form of Laplace's equation

$$\frac{1}{r}\frac{\partial}{\partial r}\left(r\frac{\partial}{\partial r}\hat{\phi}\right) + \frac{1}{r^2}\frac{\partial^2}{\partial \theta^2}\hat{\phi} + \frac{\partial^2}{\partial z^2}\hat{\phi} = 0 \qquad (20)$$

leading to

$$\frac{1}{r}\frac{\partial}{\partial r}\left(r\frac{\partial}{\partial r}\hat{\phi}^*\right) - \frac{m^2}{r^2}\hat{\phi}^* + \frac{m^2}{r^2}\hat{\phi}^* = 0. \qquad (21)$$

The derivatives with respect to θ and z cancel, leaving only the first term. Expansion of the first term yields

$$\frac{1}{r}\frac{\partial}{\partial r}\left(r\frac{\partial}{\partial r}\hat{\phi}^*\right) = \frac{mz}{r^3}\hat{\phi}^* + \frac{m^2 z^2}{r^4}\hat{\phi}^*. \qquad (22)$$

This term cannot be zero for all nontrivial physically significant values of m, z, and r, so the entire left side of (21) cannot vanish as desired. The entire term of (22) must be small compared to the second and third terms in (21) if the dominant balance of those two terms is to be preserved, which must happen for the coordinate system approximation to be valid. Therefore, in order for a model that is based on the approximation underlying (19) to be accurate, energy stored in the fields must be significant only in regions that satisfy

$$\frac{mz}{r^3} \ll \frac{m^2}{r^2} \qquad (23)$$

and

$$\frac{m^2 z^2}{r^4} \ll \frac{m^2}{r^2}. \qquad (24)$$

This leads to the two conditions

$$z \ll mr \qquad (25)$$

and

$$z \ll r. \qquad (26)$$

Since m will not be less than unity, (26) is most demanding. This is easily satisfied by all designs considered here, which have minimum radii on the order of 1 mm and fields that vanish well within 100 μm in the z-coordinate direction, even when those fields are not limited by the higher conductivity substrate layers. Thus, from here on $\hat{\phi}^*$ will be used to approximate $\hat{\phi}$, but the superscript * will be dropped for notational simplicity.

Using the coordinate transformation and related rules in Fig. 6(d) to transform f_y into τ, the torque on the rotor is expressed as

$$\boldsymbol{\tau} = \int_{R_i}^{R_o} r f_y \cdot 2\pi r dr = \varepsilon_g \pi V^2 \int_{R_i}^{R_o} \alpha(r)\beta(r)\chi(r) dr \qquad (27)$$

in which

$$\alpha(r) \equiv \frac{\Gamma(r)}{1 + \Gamma(r)^2} \qquad (28)$$

$$\beta(r) \equiv \frac{\varepsilon_g}{\varepsilon_{eff}(r)\sinh\left(\frac{mG}{r}\right)} \qquad (29)$$
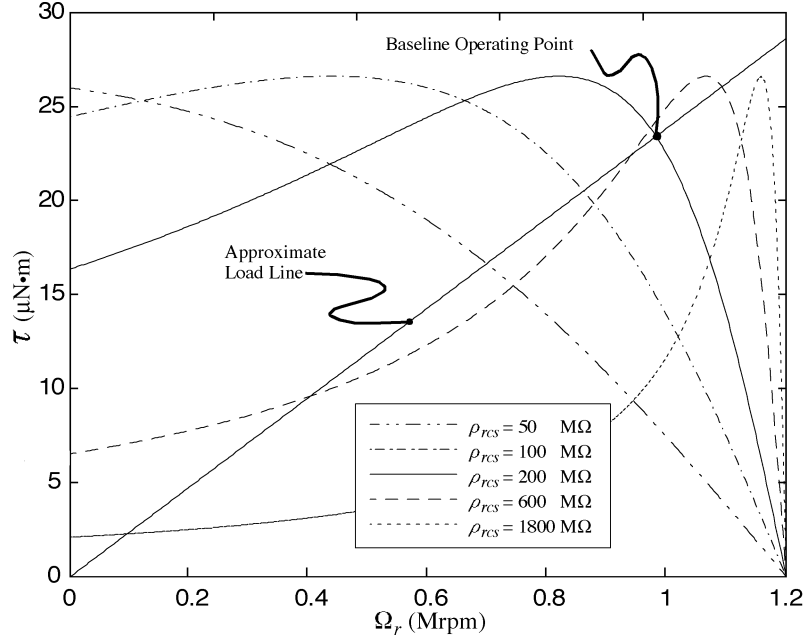
Fig. 7.   Torque versus rotor speed for several rotor conductor sheet resistances. Stator excited at the rated voltage $V_s = 300$ V and frequency $f_e = 2.6$ MHz.

and

$$\chi(r) \equiv \frac{m^2}{\sinh\left(\frac{m}{r}G\right)} \qquad (30)$$

are used to facilitate discussion in the next section.

IV. DESIGN ANALYSIS

This section describes the effects of varying three design parameters in order to describe electric induction machine operation and provide general design guidelines. The discussion is in the context of the motor-compressor because the tested motors described in this paper were designed for that particular application [18]. For simplicity of discussion in this section, output torque provides the single performance metric.

The solid curve in Fig. 7 shows the expected torque of the motor as a function of rotor speed Ω_r for a fixed electrical frequency. The operating point is the speed at which the motor torque, from the bell curve, balances the resisting load torque, from the load line. The machine parameters are those of the baseline motor design given in Table I. At constant stator excitation frequency $\omega_e = 2\pi f_e$ the torque curves are anti-symmetrical about the motor-compressor synchronous speed of $\Omega_{\text{sync}} = \omega_e/m$, equal to 1.2 Mrpm for this motor. Note that the discussion here also applies to the use of the machine as a generator, though in that case a more appropriate metric might be power generated, rather than torque.

In Section VI, torque measurements are made with the tethered motor, thus the rotor is fixed and $\Omega_r = 0$. For those measurements, the independent experimental variable is the stator excitation frequency f_e and the bell curves are anti-symmetrical about $f_e = 0$ In that case, shown in Fig. 16, and in this case, shown in Fig. 7, it is the slip frequency that actually places us on the torque curves. The curves take the same shape in both cases, described by (27). We use Ω_r here and f_e only because

we happen to find these labels more descriptive. It so happens that when the rotor is fixed, f_e is equivalent to slip frequency.

Maximum torque is the result of a balance between charge convection and charge relaxation. Charge convection is governed by the speed of the rotor, while charge relaxation is a function of machine capacitance and rotor resistance, as described in (7)–(15). The competition between convection and relaxation is captured in $\alpha(r)$ and illustrated by the torque curves in Fig. 7. Changes in convection, through changes in rotor speed, are plotted along the horizontal axis, while the sequence of distinct bell curves for various rotor sheet resistance values shows the effect of changes in the charge relaxation time. If the stator excitation frequency is fixed, as in Fig. 7, the best value of rotor resistance results from a compromise between two design goals: high starting torque and high operating speed. Maximum torque remains constant during that compromise, it is always found where convection and relaxation are in balance, which is found when $\Gamma = 1$ and occurs at a rotor speed given by

$$\Omega_{max} = \frac{\omega_e - \frac{1}{\tau_R}}{m}. \qquad (31)$$

Note that according to (31) if the charge relaxation time increases, for example if the rotor conductor sheet resistance increases, then the speed of maximum torque increases as illustrated in Fig. 7. This equation also demonstrates that if the stator excitation frequency is not fixed, then the speed of maximum torque can be actively controlled such that maximum torque is available at all rotor speeds.

Due to the required high voltage and high frequency, a fixed frequency power electronic drive would most likely be used in a practical realization of a higher power machine. Therefore, a rotor conductor sheet resistance ρ_{rcs} of 200 MΩ is chosen as an adequate compromise between starting torque and operating speed at peak torque. Also, for a fixed drive the shape of the torque curve can be critical. Though this aspect is not discussed further, the reader can see from Fig. 7 that higher
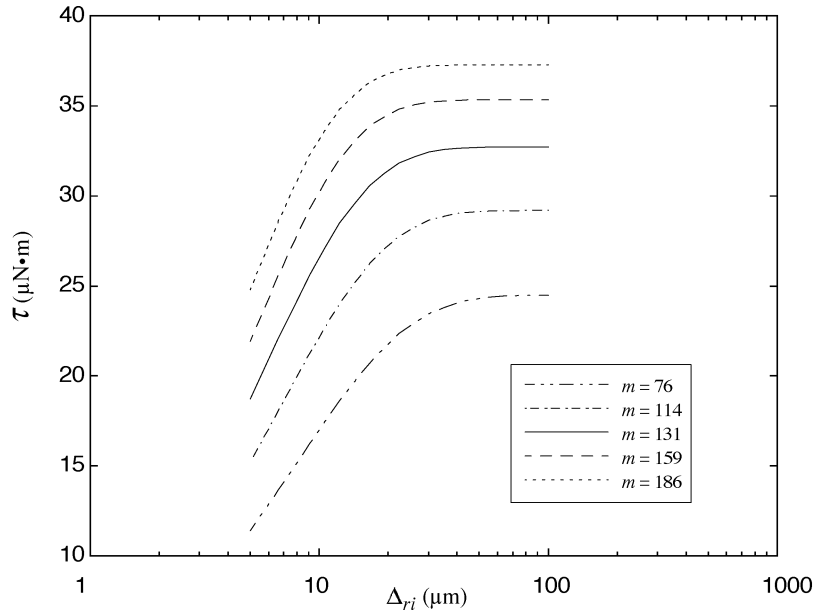
Fig. 8. Maximum torque plotted as a function of rotor insulator thickness, for several values of m. Stator excited at a voltage $V_s = 300$ V and frequency $f_e = 2.6$ MHz.

sheet resistances such as 600 and 1200 $M\Omega$ would result in much lower operating speeds of about 0.4 and 0.1 Mrpm, respectively, and lower torque, rendering the available high maximum torque unusable. Finally, rotor insulator resistivity ρ_{ri} is not mentioned here because it is infinite in comparison to the rotor conductor sheet resistance, making it irrelevant. For a lower resistance rotor insulator, changes in it's resistivity are analogous to changes in the rotor conductor resistivity.

Additional physical and fabrication considerations lead to the rest of the baseline motor design parameters in Table I. Three parameters in particular have a strong effect on the performance of the motor. First, torque is inversely proportional to the air gap length G. Second, torque first increases dramatically with rotor insulator thickness Δ_{ri}, after which there are diminishing returns. Finally, torque is initially proportional to the number of electrodes, after which, again, there are diminishing returns. The following discussion of trends in these parameters focuses on the maximum torque achieved by the solid line in Fig. 7. Most of the remaining parameters in Table I either do not significantly affect torque, or are constrained by the intended application [2]. Where unconstrained, they are chosen for fabrication simplicity.

It is straightforward to increase torque by decreasing the air gap, but there is a limit. The design air gap length has been chosen through a combination of the desired stator excitation voltage, dictated by limits on the electronics, and the breakdown strength of air in micron-sized gaps, dictated by electrode topology and material. Viscous drag also increases as the air gap decreases, but it is within acceptable limits for air gaps near our design. For primarily electrical breakdown reasons the air gap is chosen to be 3 μm based on the stator rated voltage $V_s = 300$ V, limited by electronics.

Conversely, the rotor insulator thickness is set by fabrication limitations. Torque decreases with decreasing rotor insulator thickness because of capacitive shunting, an effect that is captured primarily by the term β. The rotor is fabricated on a single crystal silicon substrate, which has a higher dielectric constant than the rotor insulator and a much higher conductivity. If the rotor insulator is made thinner, more charge is induced at the substrate-insulator interface at the expense of charge at the rotor conductor. Torque is produced by electric fields acting on charge at the rotor conductor, not charge at the substrate interface, therefore a thinner rotor insulator reduces torque. The summary torque benefit and eventual diminished returns of a thicker rotor insulator are shown for various periodicities in Fig. 8 and in more detail in Fig. 9. Ideally, the rotor insulator thickness should be increased to the point of diminished returns, but in our case it has been set at 10 μm, the maximum possible using single layer oxide deposition techniques available at the time of fabrication [24]. Beyond this thickness, wafer bow and warp quickly reach unmanageable levels. Beyond 30 μm, the substrate interface is sufficiently far from the fields in the air gap that no appreciable charge is induced at the substrate, therefore, increasing the thickness beyond 30 μm yields little torque improvement in this design.

Stator periodicity is also limited primarily by fabrication constraints. The initial linear dependence of torque on m seen in χ is simply a result of an increase in the density of charges induced on the rotor and, therefore, the torque producing forces between them and the charges on the stator. The magnitude and relative phase of both the charge density and electric field distributions remain fixed as their spatial wavelength is decreased with increasing periodicity. Thus the average shearing force per wavelength is unchanged with increasing periodicity. Since the force density is inversely proportional to the wavelength, which does change, the spatial rate of energy conversion increases with periodicity. Therefore the torque increases linearly for moderate periodicities when motor size is constant. In (27), χ captures the initial linear trend.

To see the trend mathematically, first note that the radial extent of the machine is large, so that mG/r is small and χ can
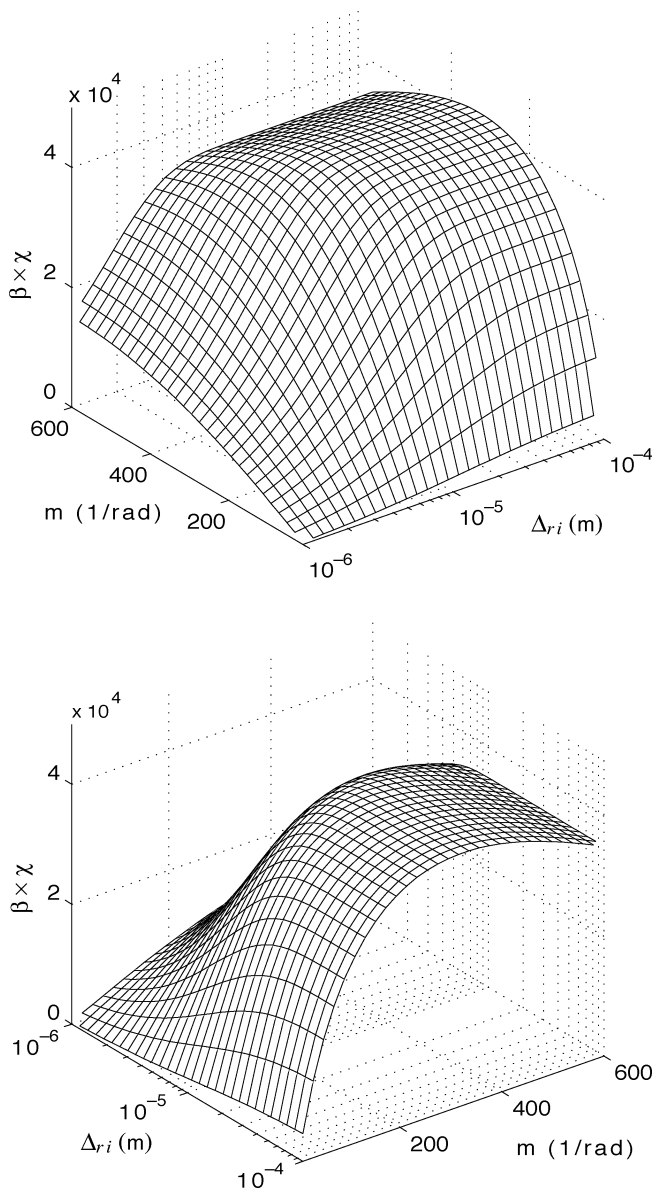
Fig. 9. The product of β and χ plotted as a function of the rotor insulator thickness Δ_{ri} and periodicity m. Stator excited at a voltage $V_s = 300$ V and frequency $f_e = 2.6$ MHz.

be approximated by mr/G. Also, $m\Delta_{ri}/r \ll mG/r$ in our design such that β has only a moderate dependence on periodicity. Next, since a rotor spinning at optimum speed makes the average Γ equal to 1, $\alpha(r)$ is considered equal to 1/2 at all radii in this simplification. Therefore in the case of small wavenumber, torque is proportional to periodicity m strictly through χ.

Several factors limit the extent to which torque is proportional to stator periodicity: field decay across the air gap that occurs with electrode-to-electrode electric field fringing, microfabrication constraints, breakdown and leakage between electrodes, and the frequency limits of the power electronics that drive the stator electrodes. The first factor is reflected in the curves in Fig. 9, through the denominator of χ, when considered along the periodicity axis. As the periodicity becomes large, the nature of the electric field in the air gap changes. First, the fields responsible for inducing charges on the rotor decay more rapidly

across the air gap so that less charge is developed on the rotor. At the same time, fringing increases. It becomes more favorable for field lines to extend from positively charged electrodes to negatively charged electrodes, rather than from charges on the electrodes to image charges on the rotor. Electrode to electrode fields will not contribute to torque. Therefore, for a machine of constant radial extent, it is not possible to increase torque ad infinitum by adding more electrodes. A point is eventually reached where the air gap must also be reduced in relation to the increase of m. Equation (27) fully captures this trend.

It so happened that the design value of m arose primarily as a result of the second and third factors: fabrication and electric breakdown concerns. Lithography considerations at the inner radius set a minimum electrode width of 4 μm, and electric breakdown constraints also suggested that the electrodes be separated by 4 μm along their entire length. Since the inner radius is 1 mm, and there are 6 electrodes and 6 spaces per stator wavelength, the periodicity m was set at 131. More aggressive fabrication techniques, for example those yielding a line width of 1 μm, and an interelectrode space of around 2 μm, could raise the periodicity by almost a factor of 3. However, the risk of electric breakdown between electrodes would increase substantially as the interelectrode gap decreased. In addition, as the electrodes become extremely narrow, high frequency operation could result in charging delay along their length. This could result in undesirable phase shifts between azimuthal sections of electrodes and would most likely result in lower peak voltages. Therefore extremely narrow electrodes could reduce torque unless they are of sufficiently high conductivity, thus motivating the use of metal electrodes.

Finally, even if all of the above concerns over an increase in periodicity are overcome, there could be higher losses in the power electronics, the fourth concern above. To maintain peak torque at a given rotation speed, the electrical frequency must increase nearly linearly with m. Inspection of (13) shows that $1/\tau_R$ is quadratic in m for small m, but becomes linear thereafter. Thus, from (31), if the design speed is to be maintained the stator excitation frequency ω_e must increase in proportion to m. Excitation electronics can be either hard switching or resonant. Both switching losses and resonant inductor losses will increase linearly with increasing frequency, becoming unmanageable at higher frequencies, given the design voltage of 300 V.

V. TETHERED MOTOR FABRICATION

This section describes the fabrication of two tethered electric induction motors, referred to as Device-1 and Device-2. The primary difference between them concerns the fabrication of their stators. The testing of these machines is reported in Section VI.

Device-1 was fabricated as outlined in Fig. 10. Its fabrication used a total of 10 masks and had approximately 160 unit-process steps. Its stator vias required alignment to within 2 μm to ensure that all electrodes would be connected to the phase buses. A 5 μm thick stator insulator, silicon dioxide, was deposited under the stator to reduce parasitic capacitance between electrodes, phase buses, and the silicon substrate. In future motors the oxide could be made thicker using a special process

Stator Wafer

1. Deposit 5 μm stator insulator.

2. Deposit 1 μm LPCVD polysilicon; implant heavily, pattern and etch phase buses.

3. Deposit 2 μm oxide; CMP; etch-back; pattern and etch vias

4. Deposit LPCVD polysilicon, implant. Deposit 1000 Å bonding oxide and CMP.

5. Wet etch to clear active area. Pattern and etch electrodes, interconnects, and wire bond pads.

Tethered Rotor Wafer

1. *Top side (TS):* Etch ID marks and measurement patterns. Deposit tether etch mask oxide; densify.

2. *Bottom side (BS):* Etch silicon pit; deposit 90% of rotor insulator; wet etch oxide not on rotor; densify. Deposit remaining rotor insulator; densify.

3. *Both sides:* Deposit LPCVD polysilicon. *BS:* Deposit implant shield oxide; anneal. Implant lightly with Boron and anneal. Wet etch to remove implant shield. Pattern and etch rotor conductor.

4. *BS:* Pattern and wet etch remaining 10% rotor insulator from field.

5. *BS:* Attach carrier wafer for through-wafer etch. *TS:* Blanket etch polysilicon layer; pattern and etch tether mask oxide.

6. *TS:* Deep RIE tethers and rotor disk; remove carrier wafer.
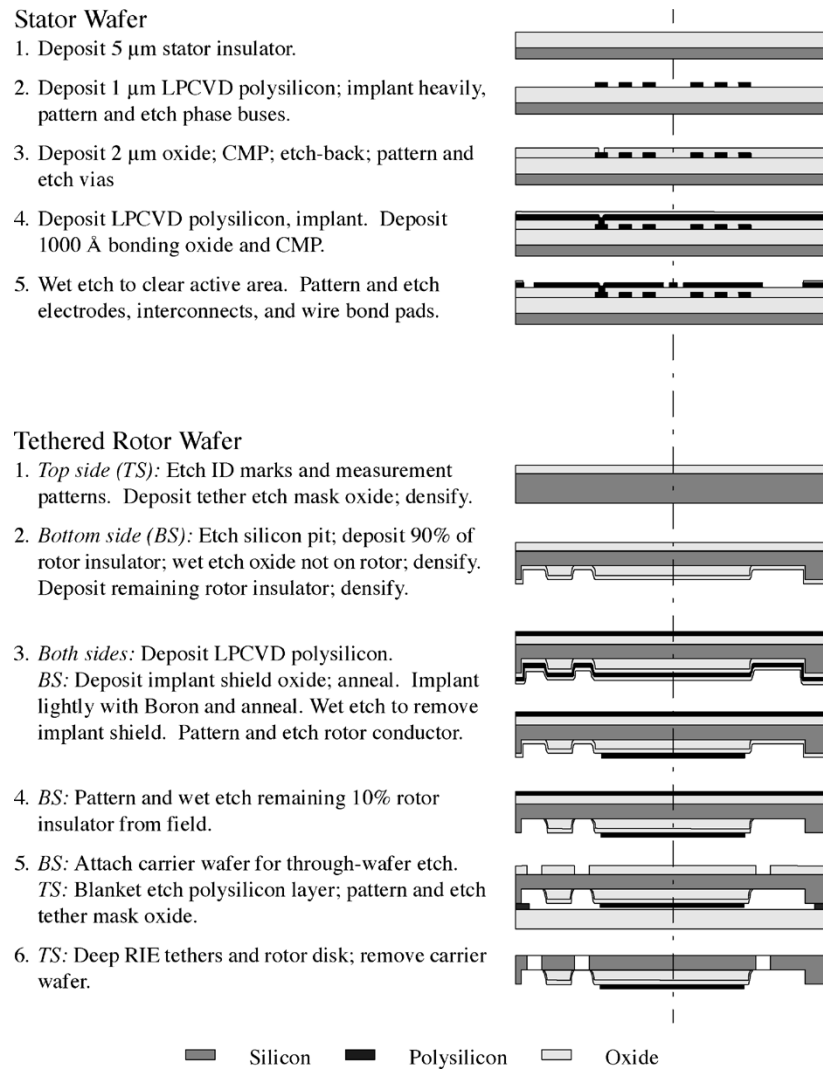
▭ Silicon   ▬ Polysilicon   ▭ Oxide

Fig. 10. Simplified process flow description for a tethered motor. For clarity, thicknesses have been exaggerated and only three phase buses are shown.

to manage the wafer bow from thermal mismatch between silicon dioxide and silicon. A thick insulator reduces reactive currents and the associated resistive losses in all conductors in the stator—phase buses, electrodes, and interconnects from electrodes to wire bond pads—and in the drive electronics, thereby improving overall efficiency. Losses still exist, but they can be overcome when using the electric induction machine as a motor. The same losses are too great for operation as a generator.

Since the ultimate goal of the electric induction machine within the tethered motor is to operate as a generator, the Device-2 stator was fabricated in a substantially different fashion. The stator of that device was fabricated on a quartz wafer, and its conductors were made of platinum, rather than heavily doped polysilicon. This fabrication process had two distinct advantages. First, parasitic capacitance was eliminated by eliminating the silicon substrate ground plane, thereby reducing reactive currents and the associated internal and external resistive losses. Second, internal losses in the phase buses, electrodes, and interconnects were further reduced since platinum is a much better conductor than heavily doped polysilicon. With these changes it is conceivable to use the electric induction machine as a generator. As a bonus, residual stresses

were eliminated since both the stator insulator and the substrate were oxide. Since there is no thermal expansion mis-match, this could make wafer bonding more practical.

Device-1 and Device-2 used nearly identical tethered rotors fabricated as outlined in Fig. 10. This process had two critical steps. First, the rotor conductor was fabricated by lightly doping a coarse-grain polysilicon film, and managing thermal treatments in the remaining fabrication. Second, the tethers were formed using a high aspect ratio DRIE from Surface Technology Systems. The aspect ratio needed to decouple azimuthal and axial beam bending forces resulting from the application of the electrical f_y and f_z forces was about 50:1, resulting in tethers 8 μm wide and 386 μm tall.

Device-1 and Device-2 were both hand-assembled. Device-1 was hand-assembled from individual stator and rotor die using high temperature H2OE metallic epoxy from Epoxy Technologies, Inc. This epoxy enabled high-temperature wire bonding, needed for direct wire bonds to the polysilicon wire bond pads. Unfortunately the epoxy wicked between the rotor die and the stator die, which was bowed by thick oxide stress. This in turn resulted in a substantially increased air gap as will be discussed in Section VI. The stator and rotor die of Device-2 were held to-
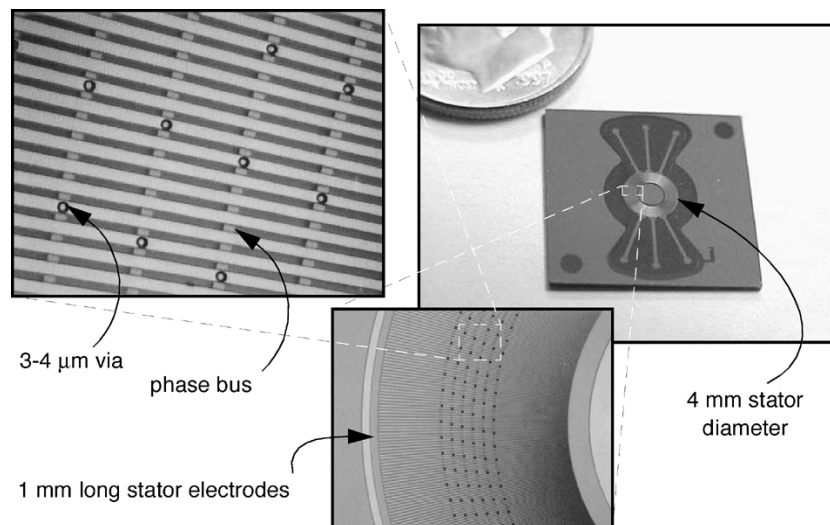
Fig. 11. Representative pictures of a tethered motor stator like that in Device-1. Note the alignment of the vias, phase buses (vertical in upper left picture), and electrodes (horizontal in upper left picture).
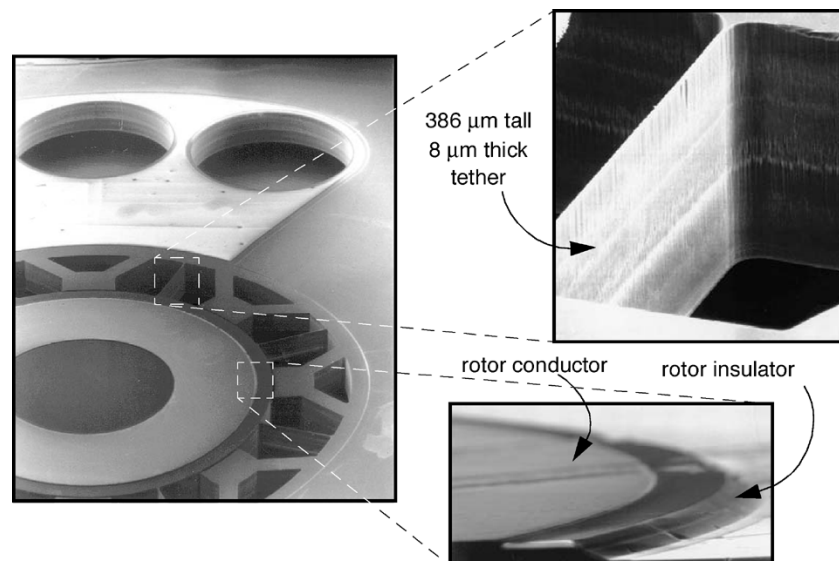

Fig. 12. Representative pictures of a tethered motor rotor like that in both Device-1 and Device-2. Note the thin tethers (left and upper right pictures), the thick rotor insulator, and the rotor conductor on top of the rotor insulator (lower right picture).

gether by clamps. Electrical contact to the platinum wire bond pads was made via spring-loaded pins. Both devices looked much like the simplified illustration of a tethered motor shown in Fig. 1. Representative SEM pictures of a silicon substrate stator are shown in Fig. 11 and pictures of a rotor are shown in Fig. 12. A picture of Device-1 is shown in Fig. 13.

VI. TETHERED MOTOR EXPERIMENTAL RESULTS

Torque from the tethered motor is measured by alternately driving the stator potential wave forward and backward around the stator annulus. This results in a square wave of torque applied to the rotor, which vibrates the spring-mass system that is made up of the tether springs and the rotor mass. The resulting periodic rotor displacement is then directly measured using a computer microvision system [14] as the torque-re-versal vibration-frequency is swept through the resonance of the spring-mass system. The computer microvision system uses

high speed video to record and measure the periodic displace-ment of the tethered rotor. Typical displacement amplitude data in Fig. 14 shows that the tethered motor is not a linear second-order system, nevertheless a tether spring-constant and the torque can be extracted (in a manner described later). Next, the vibration frequency is swept through the same range for a variety of stator excitation frequencies, resulting in torque measurements for various speeds at which the stator potential wave travels around the stator annulus. This produces the characteristic induction motor bell curves shown in Fig. 16. Note that this experimental procedure involves two independent frequencies. The first frequency is the electrical frequency ω_e of the stator excitation. The second frequency ω_v is the frequency at which the travel direction of the stator potential wave is reversed.

Typical raw displacement amplitude data is plotted in Fig. 14, clearly showing that the tethered motor is not a linear second-
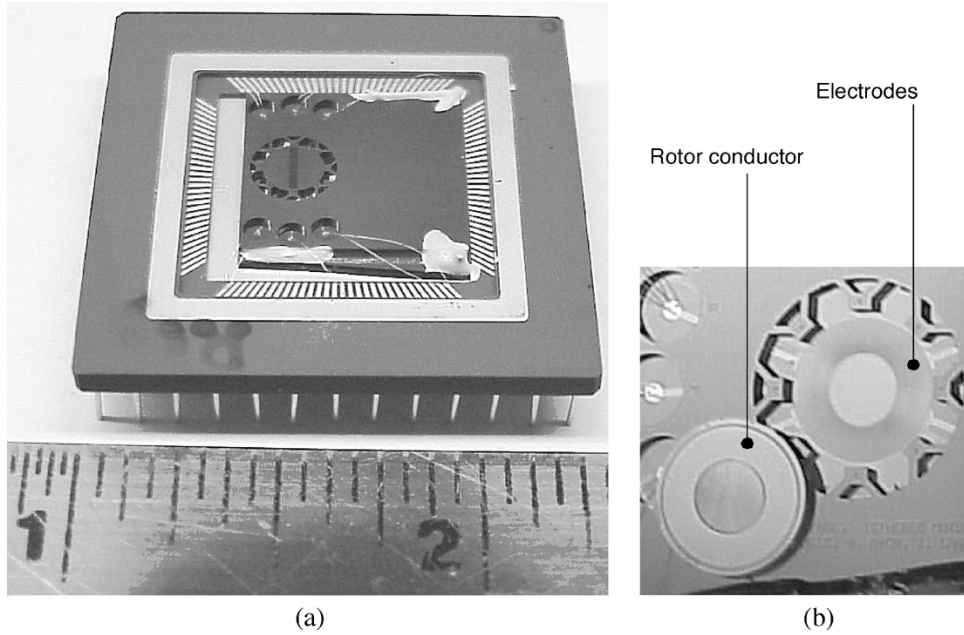
Fig. 13. (a) The first tethered electric induction motor, Device-1 (ruler in inches). (b) Another motor whose rotor has been taken out and laid upsidedown on top of the stator.
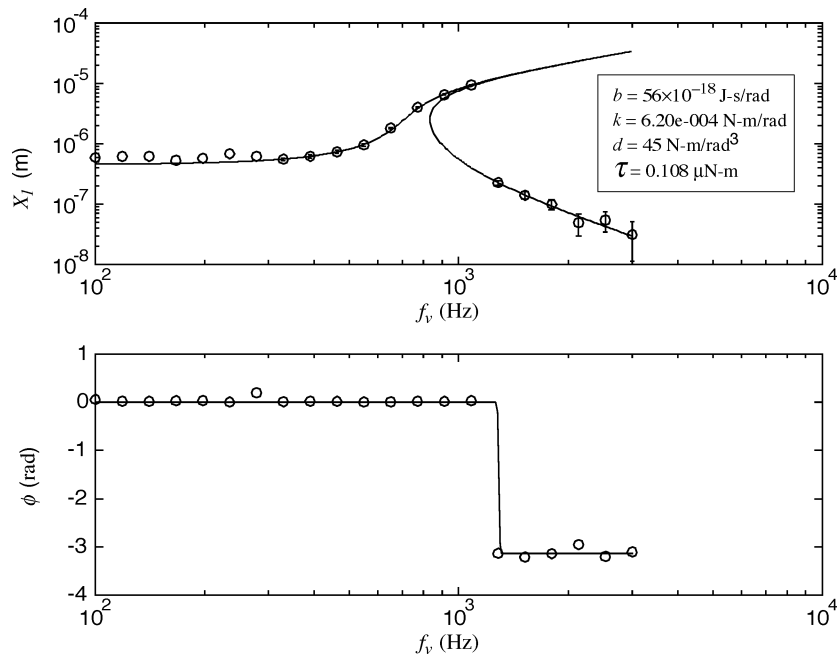

Fig. 14. A plot of rotor perimeter tangential displacement amplitude versus vibration frequency as measured by the microvision system for $f_e = 100\,\text{kHz}$ and $V = 80\,\text{V}$. X_1 is the fundamental fourier harmonic of the tangential displacement of the perimeter of the rotor. The solid curve was fit to the data using the parameters in the legend.

order system. As a result of using dual-cantilever rectangular-cross-section-beam springs firmly anchored to the rotor at one end and to a rigid support at the other, the tethered rotor behaves as a Duffing oscillator [15], [21]. This is a cubically nonlinear second-order system described by

$$j_r \ddot{\theta} + b\dot{\theta} + k\theta + d\theta^3 = \tau_j(t). \tag{32}$$

Here the deflection angle θ is given by $\theta = x(t)/R_r$ where $x(t)$ is the measured tangential displacement of the rotor at radius R_r. The moment of inertia of the rotor is given by $J_r = (1/2)M_r R_r^2$, where M_r is the mass of the rotor and R_r is the

outer radius of the tethered rotor disk. Viscous damping enters through b; k is the linear spring stiffness; and d is the cubic spring stiffness. The forcing torque is $\tau_f(t)$, whose time functionality is set by the excitation electronics. Since the rotor is vibrated by reversing the direction of the stator excitation, the torque forcing function is a square wave, expressed here as

$$\tau_f(t) = \tau(\omega_e, V) \sum_{n=1}^{\infty} \frac{4}{n\pi} \cos(n\omega_v t) \tag{33}$$

where $\omega_e = 2\pi f_e$ is the stator electrical frequency and $\omega_v = 2\pi f_v$ is the fundamental rotor vibration frequency in which τ is
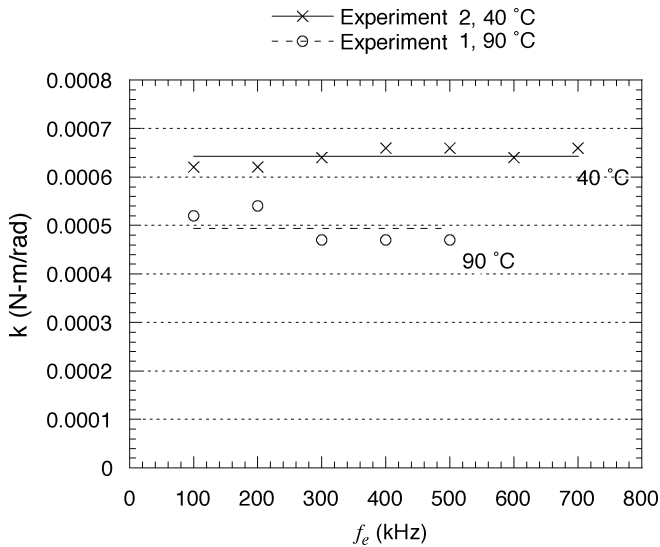
Fig. 15. Fitted linear stiffnesses for Experiments 1 and 2. Note the increase in stiffness as the tethered motor temperature decreased from 90 °C in Experiment 1, to 40 °C in Experiment 2.

defined by (27). Displacement harmonics other than the fundamental are neglected in the analysis later. Due to the nonlinearity of the Duffing equation, each torque harmonic excites several displacement harmonics. These higher order motion harmonics cause only small-scale scatter in the low vibration frequency data [15].

Torque is extracted by fitting (32) to the fundamental component of the observed rotor motion versus vibration frequency for each combination of applied ω_e and V, the latter calculated according to Section III from measured voltages applied to the stator. The rotor inertia is known by weighing five identical rotors and averaging the results. The damping coefficient is estimated at $b \cong 56 \times 10^{-18}$ J $-$ s/rad by fitting a linear second-order system to small amplitude deflection data, in which case the cubic term is negligible. Given b and J_r, the fitting parameters are then the cubic and linear tether spring constants, and the fundamental of τ_f. In the figures and in the following discussion, the term measured torque will refer to τ, calculated as $\pi/4$ times the fundamental of τ_f using (33). Fig. 15 shows spring constants fitted to data from Device-1, and Fig. 16 shows measured torques, each plotted versus the stator excitation frequency f_e for Experiments 1 and 2. The two different experiments were performed at different temperatures.

The measured torque from Device-1 in Experiments 1 and 2 is compared in Fig. 16 to the model from Section III. In each trial that produced a measured torque data point, the applied stator voltage was measured at the output of the excitation electronics. Measured torque is then normalized with respect to the greatest measured torque in an experiment through the following procedure: The torque in each trial is multiplied by the squared ratio of (a) the spatial and temporal fundamental stator voltage harmonic V for that trial, calculated from the applied voltage measured at the electronics, to (b) the fundamental voltage V in the trial of greatest torque, which had also been measured at the electronics. Only when normalized to a common excitation voltage can all data points be fit by one bell curve as described later.

In addition, the excitation electronics deliver nonsinusoidal temporal waveforms to the electrodes, so the stator voltage waveforms contain multiple harmonics in both space and time. Due to the shape of an induction machine torque curve versus stator excitation frequency, the fundamentals dominate, providing the basis for the normalization. Higher harmonics produce smaller torque maxima, and those maxima occur at multiples of the fundamental stator excitation frequency, resulting in a very small contribution to the total torque measured at each of the fundamental stator excitation frequencies in the data set. However, to fit the line shown in Fig. 16 to the data, all significant harmonics in time and space are used to produce the best possible fit of predicted performance to the measured tethered motor torque data in order to yield the best possible estimates of the air gap length and the rotor conductor sheet resistance.

Accordingly, the first three nonzero temporal harmonics from the trial of greatest torque, and the first three nonzero spatial harmonics calculated from each, are used in a single least-squares fit of the rotor conductor sheet resistance and air gap length in (27) to the normalized measured torque data. The fits are shown as the lines in Fig. 16 with fit parameters shown in the legends. Recall that in Sections III and IV the primary independent variable was rotor speed, but here it is the stator excitation frequency. All discussion from Sections III and IV is applicable to the results in Fig. 16. In a sense the curves are merely reversed when compared to Fig. 7. Close inspection of (10), (12), and (27) shows why this is.

Device-2, measured in the same manner as Device-1 in a single trial in Experiment 3, produced torque more than one order of magnitude higher, at 2 ± 0.6 μmN $-$ m. The stator was driven using a voltage fundamental $V = 90$ V at an excitation frequency of 300 kHz, and torque reversal frequencies were comparable to those used in Experiments 1 and 2.

Experiments 1 and 2 strongly suggest that the Device-1 rotor conductor resistance and air gap are both greater than their design values. Though not directly confirmed by these experiments, the measurements and theory indirectly support the hypothesis. Consider the air gap length first. As was noted in Section V, during the hand assembly process epoxy wicked between the stator and rotor die. Closer inspection showed that only one side of the motor was affected, so that on the other side the stator die and rotor support structure make direct contact. Using this point of reference, a precision microscope stage, and a lens with a shallow depth of focus, the wedge error between the stator and rotor surfaces were readily measured. The air gap varied from 4 μm to 20 $\pm$ 2 μm across the rotor, rather than holding steady at the intended 3 μm. Since torque is inversely related to the air gap length, this results in an effective air gap length of 13 $\pm$ 2 μm. This compares well with 11 μm predicted from the measured torque data presented above.

Next, consider the rotor conductor resistance. First, recall that the epoxy was metallic. Electrical measurements concluded that one of the six stator phases was shorted by the epoxy. On one hand, this was unfortunate because it decreased torque. On the other hand, it allowed the tethered motor to be heated, which allowed the rotor resistance to be altered. Thus the shorted stator phase was used as a resistive heater by applying to it a specific
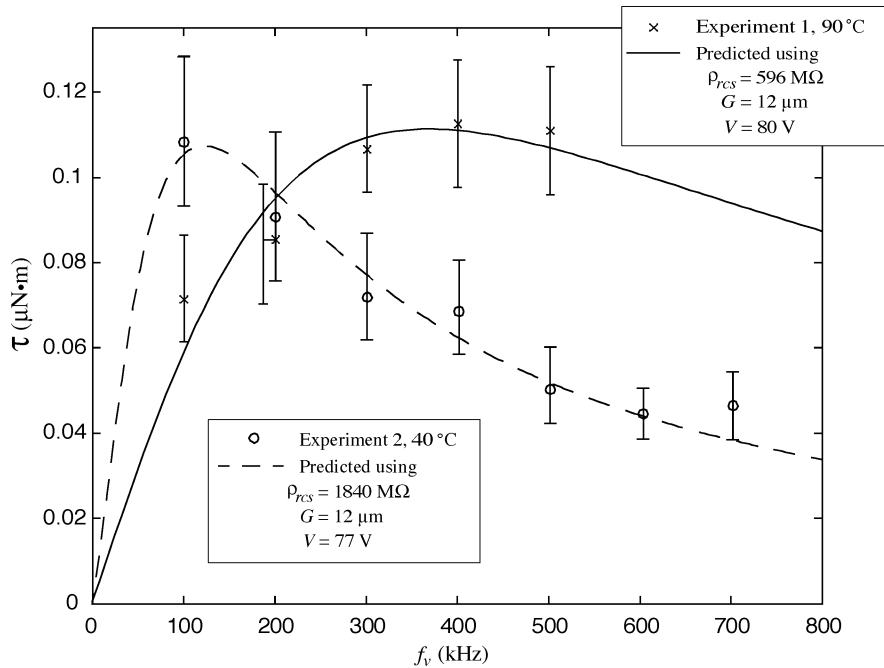
Fig. 16. Plots of measured torque versus stator excitation frequency, for two rotor temperatures, with simulated torque curves fit by the method of least-squares.

constant voltage. By monitoring the linear thermal expansion of the tethered motor, in particular the metallic portions of its package, the temperature of the tethered motor was raised from room temperature to about 40 °C in Experiment 1 and to about 90 °C in Experiment 2 [16]. (Experiment 3 was carried out at 20 °C, room temperature.) In this way, the shorted phase enabled a change in rotor conductor resistance because the resistivity of lightly doped polysilicon is a strong function of temperature. Fig. 17 plots the fitted rotor conductor resistivity versus inverse temperature for this rotor conductor and shows the governing equation as a solid line [17]. The fitted activation energy compares well with that expected from the implant dose of 5.5×10^{12} ions/cm^2 if an ion activation efficiency of about 90% is assumed. This is high but not unreasonable. Extrapolation to room temperature would yield a rotor conductor sheet resistance of 3300 MΩ per square.

Although more, and more accurate, temperature data would be needed to make a definitive statement about the actual room temperature sheet resistance, the higher room-temperature rotor conductor sheet resistance, compared to the design value shown in Table I, could be the result of the absence of a fusion bond that should have been employed to join the rotor and stator. Although grain growth primarily occurs during the anneal after implant, it continues during other high temperature processing and affects resistance. Supreme-III polysilicon deposition and growth calculations predict that in a film that had only the post implant anneal, grains would grow by a factor of 10 during the next 1100 °C anneal. Had a fusion bond been carried out as intended, this would have decreased the rotor resistance by approximately one order of magnitude [17]. Since the fusion bond was not carried out for the tethered motor of Experiments 1 and 2, the grains never grew, and it is entirely reasonable that the rotor resistance was about an order of magnitude higher than designed, as observed.
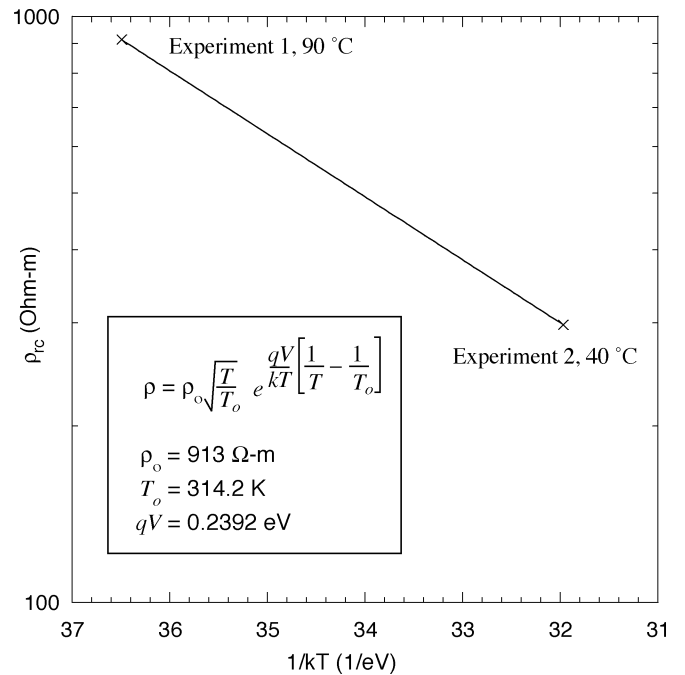

Fig. 17. Variation in rotor conductor resistivity with rotor temperature, deduced from the torque measurements of Experiments 1 and 2. See [17] for the origin of the resistivity equation, from which the solid line was drawn.

VII. CONCLUSION

This paper offers several advancements to the science and engineering of micromotors. To begin, this paper presents the practical design and fabrication of an electric induction micromotor. The design is optimized for fabrication in the MIT Microsystems Technology Laboratories. The primary limiting constraints of this design are the minimum feature sizes of the air gap and the stator electrodes, as well as the electrode spacing, and

the maximum thickness of the stator and rotor insulators. Next, this paper introduces the concept of a tethered micromotor as a torque measurement device. Finally, this paper presents tests of two tethered electric induction micromotors, with one micromotor tested over a wide range of stator excitations to demonstrate that it performs as expected from basic theory. This paper demonstrates a micromotor with a torque in excess of $2\,\mu\mathrm{N}\cdot\mathrm{m}$.

In closing, it is interesting to note that the electrical excitation, and hence the torque reported in Experiment 3 was limited by the fact that the tethers broke when trying to increase torque. The torque was not limited by electrical breakdown within the micromotor. The rated voltage of the micromotor is actually 300 V, and the stator has been demonstrated to routinely withstand this voltage. Therefore, computing the voltage fundamental in the manner of Section III, the rated torque of the Device-2 micromotor is $2\,\mu\mathrm{N}\cdot\mathrm{m} \times (285/90)^2 = 20\,\mu\mathrm{N}\cdot\mathrm{m}$. At a speed of 2.4 Mrpm, as is planned in [2], its rated motoring (or generating) air gap power would then be 5.5 W. The micromotor therefore compares well with macroscale magnetic integral horsepower industrial motors on performance metrics like the shear stress on the rotor. The maximum shear stress attained by the tethered electric induction motors is about $140\,\mathrm{N/m}^2$ at reduced stator voltage. If these results are scaled up to full voltage, the shear stress would be about $1400\,\mathrm{N/m}^2$, as compared to about $7000\,\mathrm{N/m}^2$ for a typical integral horsepower magnetic induction motor [27]. Thus, the elevated electric field strength made possible by the use of a narrow air gap permits a micro-scale electric machine to perform nearly as well as a macroscale magnetic machine.

References

[1] A. H. Epstein and S. D. Senturia, "Macro power from micro machinery," *Science*, vol. 276, p. 1211, May 1997.

[2] A. Epstein *et al.*, "Power MEMS and microengines," in *Transducers 97; 1997 Int. Conf. Solid-State Sens. Actuators, Dig. Tech. Papers*, vol. 2, 1997, pp. 753–756.

[3] E. J. Garcia and J. J. Sniegowski, "Surface micromachined microengine," *Sens. Actuators A*, vol. A48, no. 3, pp. 203–214, May 1995.

[4] B. Makin and B. J. Coles, "Novel electrostatic micromotors," in *Proc. Sixth Int. Conf. Elect. Machines and Drives*, 1993, Conf. Publ. 376, pp. 1–3.

[5] J. Melcher, *Continuum Electromechanics*. Cambridge: MIT Press, 1981, pp. 5–45.

[6] B. Bollée, "Electrostatic motors," *Philips Tech. Rev.*, vol. 30, no. 6/7, pp. 178–194, 1969.

[7] S. D. Choi and D. A. Dunn, "A surface-charge induction motor," *Proc. IEEE*, vol. 59, no. 5, pp. 737–748, May 1971.

[8] P. T. Krein and J. M. Crowley, "Harmonic effects in electrostatic induction motors," *Elect. Mach. Power Syst.*, vol. 10, no. 5–6, pp. 479–497, 1985.

[9] E. R. Mognaschi and J. H. Calderwood, "Asynchronous dielectric induction motor," *IEE Proc. -A-Science Measure. Technol.*, vol. 137, no. 6, pp. 331–338, Nov. 1990.

[10] C. Kooy, "Torque on a resistive rotor in a quasi electrostatic rotating field," *Appl. Scientif. Res.*, vol. 20, no. 2–3, pp. 161–172, Feb. 1969.

[11] J. Ubbink, "Optimization of the rotor surface resistance of the asynchronous electrostatic motor," *Appl. Scientif. Res.*, vol. 22, no. 6, pp. 442–448, Oct. 1970.

[12] S. F. Bart and J. H. Lang, "An analysis of electroquasistatic induction micromotors," *Sens. Actuators*, vol. 20, pp. 97–106, Nov. 1989.

[13] J. F. Charpentier, Y. Lefevre, E. Sarraute, and B. Trannoy, "Synthesis and modeling of an electrostatic induction motor," *IEEE Trans. Magn.*, vol. 31, no. 3, pp. 1404–1407, May 1995.

[14] D. M. Freeman, A. J. Aranyosi, M. J. Gordon, and S. S. Hong, "Multidimensional motion analysis of MEMS using computer microvision," in *Solid-State Sensor and Actuator Workshop*, Cleveland, OH, 1998, pp. 150–155.

[15] N. W. McLachlan, *Ordinary Non-Linear Differential Equations in Engineering and Physical Sciences*, 2nd ed. London, U.K.: Oxford University Press, 1956.

[16] R. A. Pease, *Troubleshooting Analog Circuits*. Newton, MA: Butterworth-Heineman, 1993, p. 83.

[17] T. Kamins, *Polycrystalline Silicon for Integrated Circuits and Displays*, 2nd ed. Boston, MA: Kluwer Academic, 1998.

[18] L. G. Frechette, "Development of a microfabricated silicon motor-driven compression system," Ph.D. dissertation, MIT Dep. Aeronaut. Astronaut., 2000.

[19] S. F. Nagle, "Analysis, design, and fabrication of an electric induction micromotor for a gas-turbine generator," Ph.D. dissertation, MIT Dep. Electrical Engineering and Computer Sci., 2000.

[20] H. Woodson and J. Melcher, *Electromechanical Dynamics, Parts I and II* Malabar, FL, 1968.

[21] W. Weaver Jr, S. P. Timoshenko, and D. H. Young, *Vibration Problems in Engineering*, 5th ed. New York: Wiley, 1990.

[22] R. Arno, "Über ein Rotirendes Elektrisches Feld und Dursh Elektrostatische Hysteresis Bewirkte Rotationen," *Electrotechn Z*, vol. 14, pp. 17–18, 1863.

[23] J. H. Calderwood and R. Mognaschi, "The spatial harmonic content of the field of an electrostatic induction motor," *Int. J. Appl. Electromagn. Mater.*, vol. 6, no. 3, pp. 197–205, Nov. 1995.

[24] R. Ghodssi, L. G. Frechette, S. F. Nagle, X. Zhang, A. A. Ayon, S. D. Senturia, and M. A. Schmidt, "Thick Buried Oxide in Silicon (TBOS): an integrated fabrication technology for multi-stack wafer-bonded MEMS processes," in *Proc. 10th Int. Conf. Solid-State Sens. Actuators (Transducers 99)*, Sendai, Japan, Jun. 7–10, 1999.

[25] H. Koser, "Development of Magnetic Induction Machines for Micro Turbo Machinery," Ph.D. Thesis, MIT Dep. Elect. Eng. Comput. Sci., 2002.

[26] H. Koser, F. Cros, M. G. Allen, and J. H. Lang, "A high torque density MEMS magnetic induction machine," in *Proc.: 11th Int. Conf. Solid-State Sens. Actuators*, Munich, Germany, Jun. 10–14, 2001, pp. 284–287.

[27] T. J. E. Miller, *Switched-Reluctance Motors and Their Control*. Oxford, U.K.: Oxford University Press, 1993.

Steven F. Nagle (S'93–M'01) received the B.S. and M.S. degrees in engineering science from the Pennsylvania State University, State College, in 1994 and 1995, respectively, and received a National Science Foundation Fellowship to conduct his M.S. degree research on electromagnetic and elastodynamic wave propagation in a class of nano-structured materials. He received the Ph.D. degree from the Massachusetts Institute of Technology (MIT), Cambridge, in 2000.

He was one of the first members of the MIT Micro-Gas-Turbine Generator Team as designer of the electric starter/generator. His interests include research and development in PowerMEMS, BioMEMS, nanopackaging, and nanoprobe technology for use in scanning probe microscopy, especially self-actuated and/or self-sensing probes, and those suited for bioscience. Currently, he is the New Technology Manager for Veeco Probes, Santa Barbara, CA, a division of Veeco Instruments, Woodbury, NY.

Carol Livermore (M'99) received the B.S. degree in physics from the University of Massachusetts, Amherst, in 1993 and the A.M. and Ph.D. degrees in physics from Harvard University, Cambridge, MA, in 1995 and 1998, respectively.

From 1998 to 2002, she was a Postdoctoral Associate and then a Research Scientist with the Massachusetts Institute of Technology (MIT), Cambridge. Currently, she is an Assistant Professor with the Department of Mechanical Engineering, MIT. Her research interests include power MEMS and the development of techniques and applications for nano-, and microscale self-assembly.

Reza Ghodssi (S'92–M'97) received the B.S., M.S., and Ph.D. degrees in electrical engineering from the University of Wisconsin at Madison, in 1990, 1992, and 1996, respectively.

He was a Postdoctoral Associate and a Research Scientist in the Microsystems Technology Laboratories and the Gas Turbine Laboratory at the Massachusetts Institute of Technology (MIT), Cambridge, from 1997 until 1999. During his tenure at MIT, he developed the building block MEMS fabrication technologies for a microturbine generator device and also served as an Assistant Director on that project. He is Director of the MEMS Sensors and Actuators Laboratory (MSAL) and an Associate Professor in the Department of Electrical and Computer Engineering and the Institute for Systems Research (ISR) at the University of Maryland (UMD). He is also a core faculty member in the Bioengineering Graduate Program and Small Smart Systems Center (SSSC) at UMD. His research interests are in design and development of microfabrication technologies and their applications to microsensors, microactuators, and integrative microsystems.

Dr. Ghodssi was awarded the 2001 UMD George Corcoran Award, 2002 National Science Foundation CAREER Award, and the 2003 UMD Outstanding Systems Engineering Faculty Award. He has served as a Program Co-Chairman for the 2001 International Semiconductor Device Research Symposium (ISDRS) and as a Chairman of the MEMS and NEMS Technical Group at the American Vacuum Society (AVS), from 2002 to 2004. He is a Co-Founder of the MEMS Alliance Group in the greater Washington area and a member of the AVS, MRS, AAAS, and ASEE societies.

Luc G. Frechette received the Ph.D. degree from the Massachusetts Institute of Technology (MIT), Cambridge, in 2000.

He is currently the Canada Research Chair in Power MEMS and an Associate Professor of Mechanical Engineering at the Université de Sherbrooke, Québec, Canada. From 2000 to 2004, he was an Assistant Professor of Mechanical Engineering at Columbia University, NY. His research interests are in microengineering of miniature systems for energy conversion (Power MEMS), such as microfabricated heat engines and fuel cells, with activities ranging from integrated device development to fundamental microfluidics, heat and mass transfer studies in such microsystems. He also enjoys developing MEMS sensors and actuators for aerospace applications.

Dr. Frechette is a Member of the ASME and AIAA societies.

Jefferey H. Lang (S'78–M'79–SM'95–F'98) received SB, SM, and PhD degrees from the Department of Electrical Engineering and Computer Science at the Massachusetts Institute of Technology (MIT), Cambridge, in 1975, 1977, and 1980, respectively.

In 1980, he joined the faculty of MIT where he is now a Professor of Electrical Engineering and Computer Science. He served as the Associate Director of the MIT Laboratory for Electromagnetic and Electronic Systems between 1991 and 2003, and as an Associate Editor of Sensors and Actuators between 1991 and 1994. Professor Lang's research and teaching interests focus on the analysis, design and control of electromechanical systems with an emphasis on rotating machinery, microscale sensors and actuators, and flexible structures. He has written over 180 papers and holds 11 patents in the areas of electromechanics, power electronics and applied control, and has been awarded four best-paper prizes from IEEE societies. He is also the coauthor of *Foundations of Analog and Digital Electronic Circuits* (Morgan Kaufman, San Mateo, CA).

Dr. Lang is a former Hertz Foundation Fellow.